ExoJ: an ImageJ2/Fiji plugin for automated spatiotemporal detection of exocytosis

LIU Junjun[1*], VERWEIJ Frederik Johannes[2], VAN NIEL Guillaume[3, 6], DANGLOT Lydia[4, 5, 6 $], BUN Philippe[5, 6 *$]

[1] Shandong First Medical University & Shandong Academy of Medical Sciences, Jinan 250001, China

[2] Utrecht University, Faculty of Science, Department of Biology, 3584 CH Utrecht, The Netherlands

[3] Université de Paris, Inserm U1266, Institute of Psychiatry and Neuroscience of Paris, Team Endosomal dynamics in neuropathies, F-75014 Paris, France

[4] Université de Paris, Inserm U1266, Institute of Psychiatry and Neuroscience of Paris, Team Membrane traffic in healthy and diseased brain, F-75014 Paris, France

[5] Université de Paris, Inserm U1266, Institute of Psychiatry and Neuroscience of Paris, NeurImag Imaging Core Facility, F-75014 Paris, France

[6] GHU Paris Psychiatrie et Neurosciences, Hôpital Sainte Anne, Paris, France

[*] Corresponding authors, [$] Co-senior authors

Emails: ftdxfish@163.com, f.j.verweij@uu.nl, guillaume.van-niel@inserm.fr, lydia.danglot@inserm.fr, philippe.bun@inserm.fr

Keywords

ImageJ plugin, Exocytosis, Fusion, Vesicles, Live-cell imaging, pH-sensitive probe, TIRF

Abstract

Exocytosis is a dynamic physiological process that enables the release of biomolecules to the surrounding environment via the fusion of membrane compartments to the plasma membrane. Defects in exocytosis could compromise essential biological functions so that it is crucial to elucidate the fundamentals of the exocytosis mechanisms. The development of pH-sensitive optical reporters alongside Total Internal Reflection Fluorescence (TIRF) microscopy has greatly expanded the knowledge of exocytosis, allowing the assessment of individual vesicle exocytosis events on a single-cell basis. The amount of data generated by live-cell imaging approaches poses the need of an analytical tool to identify and quantify the dynamics of exocytic events with high accuracy from fluorescent time series. Manual annotation represents a time-consuming task, and prone to selection biases and human operational errors.

In this work, we report the development of ExoJ, an ImageJ2/Fiji-based plugin to automate the detection of exocytic events in single-cell studies. The pipeline of ExoJ entirely relies on a set of user-customizable parameters to identify and further quantify features of exocytic events such as the intensity, the apparent size and the duration of the process. ExoJ proposes a user-friendly interface with multiple optional tools to visualize features for individual exocytic events and/or the whole cell population events. To illustrate the capacity of the plugin, we recorded exocytic events reported by several tetraspanins (TSPANs) and vesicular soluble N-ethylmaleimide-sensitive fusion protein attachment protein receptors (v-SNAREs) proteins, coupled to pHluorin. Using ExoJ, we characterize the dynamics of the exocytic event population reported by these two families of proteins. We showcase a similar fusion intensity but significantly distinct dynamics among TSPAN subpopulation. In particular, TSPAN CD9-pHluorin subpopulation displays a fast and similar dynamics to v-SNARE populations.

ExoJ is a user-friendly plugin to detect exocytic events in a supervised manner. We designed ExoJ to be fully user-controllable at each step of the pipeline. We argue the user-oriented plugin is a useful tool to search, monitor and quantify the dynamic aspect of content release during exocytosis.

Background

Exocytosis is a fundamental biological process to convey sets of chemical information to the extracellular environment, and deliver membrane proteins and/or lipids to the plasma membrane (PM). The process consists in the transport, docking, priming and fusion of intracellular compartments to the (PM) [1], resulting eventually in the deposition of proteins and lipids into the PM and the release of their content to sustain important physiological functions, and response to external stimuli. An orchestrated spatiotemporal control of exocytosis is thus critical in the regulation of physiological and pathological processes [2–8] underlying the need to characterize the structural dynamics of the fusion machinery, the biochemical profile of the biological contents and the spatiotemporal dynamics of their release. In addition to a collection of biochemical approaches, methods using live-cell imaging of fluorescently-tagged intracellular vesicles allow for spatiotemporal monitoring and quantitative analysis of content release [9]. In particular, Total Internal Reflection Fluorescence (TIRF) microscopy is commonly used to detect single-vesicle exocytosis in single or multiple cells by monitoring the changes in the fluorescence intensity of a pH-sensitive fluorescent protein (FP) [10–14]. Besides the vesicle-specific protein marker, the choice of the FP greatly influences the monitoring of the dynamics of exocytosis steps as evidenced by others [15–18]. Taken together, the subsequent amount of data generated by fluorescent time series poses the need of a robust analysis pipeline to identify exocytic events with high accuracy. Manual annotation of each candidate exocytic event represents a time-consuming task, and is prone to selection biases. In particular, the recording of fusion event XY location to report potential intracellular hotspots, intensity which estimates the relative amount of proteins, apparent size and duration is hardly reproducible from one cell to the other. Numerous algorithms have been developed to address these challenges in a semi- [13, 19] or fully automated manner [20–23]. These solutions are, however, optimized for a particular population of vesicular cargoes [12, 13, 20–23]. Here we present Project-ExoJ (hereafter named ExoJ), a solution developed as an ImageJ2/Fiji [24] plugin that automates the reliable identification of exocytic events. We designed ExoJ to be fully user-configurable, with a graphical user interface to set up a series of parameters that define a genuine population of exocytic event according to the experimental condition including the type of vesicle and the dynamics of exocytosis fluorescent reporters. To improve user experience, we provided built-in tools for visualizing and further reporting features of single exocytic events such as the XY location, intensity over time, size and duration.

Implementation

Installation and system requirements

ExoJ was developed as an ImageJ2/Fiji [24] plugin for the automated detection and analysis of exocytosis events in 8 or 16-bit grayscale fluorescent image series. The plugin is published under the GPLv3 license. It uses ImageJ2/Fiji capabilities to open a wide range of image formats using the plugin Bio-Formats [25].

To install the plugin, place the .jar file in the ImageJ2/Fiji plugin directory. After a restart, ExoJ will be available in the ImageJ2/Fiji plugin menu. The plugin ExoJ is compatible with ImageJ v1.53s or newer version, and has been tested on Windows and MacOS platforms. We recommend using a 64-bit operating system and at least 4GB RAM with Java 8 installed.

Overview of the framework

We focused on the identification of fluorescently-labeled vesicle fusion to the PM (hereafter termed as fusion event) to report exocytosis. The content and/or the vesicle membrane are labeled with a pH-sensitive FP. At least three modes of exocytosis have been identified (full-collapse, kiss-and-run and compound exocytosis) and characterized according to their fusion dynamic patterns [26]. Although each mode has its own fluorescence fluctuation pattern, the fluorescence intensity decays to a certain extent right after vesicle fusion to the PM. This makes automatic recognition possible. Hence, we describe a fusion event as a transient diffraction-limited or large object that displays a sudden increase followed by an exponentially decreasing fluorescence intensity into the background (Figure 1A). With this definition, we designed our plugin to automate the robust identification and analysis of fusion events. All the parameters used for the identification of fusion events can be manually adjusted, including the apparent size, the duration, the intensity (Figure 1). This ensures our plugin to be adaptive in detecting fusion events of different dynamics. These parameters can be saved and called during any step of the procedure (Table 1). We provide tables that describe the parameters, tools and options available for each step (Tables 1-4). The framework of our algorithm consists of three major steps (Figure 1A) detailed below.

Vesicle detection

The first step consisted in detecting vesicles seen as bright spots (Figure 1B; Table 2). Our plugin reads the metadata of the selected image series to extract the pixel size, the frame rate and time interval. Users can check and correct the metadata if necessary. The main challenges posed by reliable vesicle detection are associated with prolonged live-cell acquisition, such as cell migration, focus drift and photobleaching. While cell migration and focus drift lead to unpredictable fluorescent changes at a given pixel, the photobleaching effect can be theoretically compensated to a certain extent [27]. The variations of fluorescent signals over time within cell compartments are, however, occurring at slower dynamics compared to single fusion events. To account for this, we provided a correction option, described in the section Materials and Methods. If "Correct photobleaching" is selected in the setting menu, the correction is applied on the whole time series and can be reversed upon deselection.

To detect fluorescent spots from image series, we applied the multiscale à trous wavelet transform algorithm [28] for a user-defined range of vesicle size (Min. and Max. vesicle radius). After transformation, the pixel values of single fluorescent images were equal to wavelet coefficients $C_{wavelet}$ as previously defined by [28]. To selectively keep spots within single frames of the timeseries, we defined a single hard threshold parameter $k\sigma_{wavelet}$ with $\sigma_{wavelet}$ calculated from the median absolute deviation (MAD) of $C_{wavelet}$ as follows:

$$\sigma_{wavelet} = median\,(abs\,(C_{wavelet} - median\,(C_{wavelet})))$$

The MAD is a measure of variability similar to standard deviation but less sensitive to outliers (e.g. non-specific cell compartments, noise saturated pixels, …). Hence, the sensitivity of the spot detection algorithm is imposed by users when setting the value of k. Thus, the algorithm removes the structures with $C_{wavelet}$ lower than $k\sigma_{wavelet}$ (Figure 1B). Upon activation, the option "Show lowpass image" displays the result of the à trous wavelet transform algorithm on single frames. Alternatively, users can rely on the *local maxima* algorithm (unchecked Wavelet Filter box; Figure 1B), characterized by $k\sigma_F$ where σ_F is now obtained from the MAD of pixel intensity at each image. For both algorithms, we suggest adjusting the threshold parameter when the imaging condition as well as the labeled vesicular population changes. The detection result on single images can be previewed to ensure that proper fluorescence spots were accurately detected (Figure 1B; Table 2).

Once determined, the parameter is applied for the whole image series to extract the XY location of all fluorescent spots with a local maxima method within an adaptive window sized to 2*Min. vesicle radius + 1.

Vesicle tracking

The second step consisted in building individual time-lapse trajectories of previously localized fluorescent spots (Figure 1C; Table 3). While the starts of single trajectories are due to the appearance of a bright spot, the ends are not solely due to the fusion to the PM but could result from limitations in imaging conditions (e.g. low signal-to-noise ratio, out-of-focus, …). To account for this caveat, we combined a simple but yet sufficient multi-frame nearest-neighbor approach with a gap closing algorithm [29, 30]. Here, our plugin introduces three cut-off parameters that need to be tailored according to vesicle behavior, consisting of a spatial searching range, a temporal searching depth and a minimal event size (Figure 1C, Table 3). Spot size, direction and intensity are not considered during the frame-to-frame tracking process. Spots within the user-defined spatial and temporal searching range are assigned to the same trajectory, minimizing their global lateral displacement. If the "Show event list" is activated, single detected trajectories with a user-specified minimal number of linked (i.e. detected) spots can be reviewed (Figure 1C). For each individual track, intensity profile and trajectory movie are displayed upon selection.

Fusion event identification

Various features have been considered to streamline the accurate identification of positive fusion events in different cellular contexts as compared to other types of events (e.g. kiss-and-run). Here, we combine advantages of previous methods to define a robust and adaptive user-oriented protocol [12, 13, 20–23]. We reason that all fusion events display a statistically significant and transient fluorescence peak fluctuation (F; Figure 1D) above the local background, followed by an exponential fluorescence decay. Considering single vesicle trajectories, we first performed consecutive adjacent image subtraction to normalize the background fluorescence intensity [21]. This step results in a high signal-to-noise ratio 1st-order differential fluorescent image series (dF; Figure 1D). For each candidate fusion event, we calculated $\sigma_{dF_intensity}$ as the MAD of dF instead of solely considering the normalized peak change in fluorescence intensity ($\Delta F/F_0$) [13, 19, 22]. To refine the estimation of $\sigma_{dF_intensity}$, the trajectories of single candidate events are extended before (resp. after) the appearance (resp. disappearance) of the vesicle according to user entries

(Expanding Frames; Figure 1D; Table 4). We eventually proceeded with a moving linear regression on the fluorescence peak intensity profile to refine the onset time t_0 of candidate fusion events. This step helped considering fluorescence saturation and successive events at the same XY location. The algorithm also assessed the maximal displacement of candidate events relative to their initial XY location at t_0. Additional measurements were made by our plugin to describe the population of candidate fusing vesicles, including the mean lifetime τ which relates to the fusion dynamics and serves as a proxy for the fusion duration; the apparent size of the fusion event and the normalized peak change in fluorescence intensity $\Delta F/F_0$ which estimates the relative amount of fluorescently-labeled proteins.

To account for various dynamics of vesicle fusion and/or image series acquired under different experimental conditions, we integrated user-defined entries to modulate the definition of a fusion event and hence the identification requirements of the algorithm. In particular, candidate events with 1st-order differential fluorescence peak dF higher than $k\sigma_{dF}$ (Detection threshold; Figure 1D), limited displacements (Max. displacement), duration (Upper/Lower decay limit) and estimated size (Upper/Lower est. radius limit) at t_0 that comply with user inputs were seen as fusion events (Figure 1D). For the last two parameters, the goodness-of-fit, reported by the coefficient of determination R^2, was set as a threshold value (Min. R^2) above which events are selectively kept (Figure 1D, see parameters 3 and 7).

Once the identification parameters are set, our plugin evaluates and summarizes the information of all identified fusion events (Figure S1). Each analyzed event can be visualized as a sequence of cropped images with associated fluorescence peak intensity F, differential intensity dF and estimated radius fitting plots. We also recorded the fluorescence spreading over time associated with each vesicle fusion event (Spatial dynamics; Figure S1A) as initially proposed by [31]. We implemented the possibility to discard events using the appropriate button in the result table (Remove; Figure S1A). For instances, filipodia movement in-and-out of focus could cause the plugin to detect the tip as an event as well as extracellular debris. Similarly, candidate fusion events can be manually added and immediately reviewed (draw a circle and press Add; Figure S1A). Upon selection, the plugin will prompt the user to define the starting and ending frames of the candidate fusion event. A spatiotemporal map distribution of fusion events is available upon selection in the result table (Figure S1B), and can further be exported as an RGB image.

Materials and Methods

Reporters of fusion events in live cells

We used TSPAN and v-SNARE proteins as fusion event reporters. Specifically, we relied on TSPAN CD9, CD63 and CD81 [32–35], and v-SNARE VAMP2/synaptobrevin2 (vesicle-associated membrane protein 2) and VAMP7/TI-VAMP (vesicle-associated membrane protein 7 / Tetanus neurotoxin-Insensitive vesicle-associated membrane protein) [36–40] proteins coupled to a pH-sensitive variant of GFP named pHluorin [10]. CD9-pHluorin, CD63-pHluorin and CD81-pHluorin plasmids were constructed as previously described by Verweij and colleagues [41]. VAMP2-pHluorin was a kind gift from Dr. T. Ryan (Cornell University, USA). VAMP7-pHluorin construction was previously described [42]. We used Hela cells cultured in DMEM supplemented with 10 % FBS (Perbio Sciences; HyClone), 100 U/ml penicillin G, 100 mg/ml streptomycin sulfate and 2 mM glutamax (Invitrogen, Thermofischer Scientific). Cells at 50 % to 60 % confluence were transfected using Lipofectamine 2000 reagent (Invitrogen) on either 35-mm glass bottom petri dishes (Ibidi) scaled with 500 ng of TSPAN-plasmids or 18-mm round glass coverslips deposited in 12-well plates scaled with 1 μg of VAMP plasmid. Glass coverslips are further mounted on a Chamlide EC magnetic chamber (LCI).

Live cell imaging

Prior to imaging, cell medium was typically replaced with homemade Hepes-buffered Krebs-Ringer [43] or Leibovitz's L-15 solution (Gibco). 24 h after transfection, Hela cells were imaged on an inverted microscope (Axio Observer 7, Zeiss) equipped with a TIRF module and a top stage imaging chamber (Tokai Hit STX-CO2) ensuring a constant temperature at 37°C. All imaging experiments were carried out with a 63x 1.4 NA oil objective (Zeiss), an air-cooled 488 nm laser line at 0.4-0.6% power, with a TIRF angle set for 300-400-nm penetration depth and an additional optovar 1.6x to reach a pixel size of 100 nm. Images were acquired with Zen Black (SP2.3, Zeiss) onto an electron-multiplying charge-coupled device camera (iXon, Andor) at a frame rate of 5 Hz for 3 minutes. Fluorescent time series were saved as tiff or czi files. Fusion activity was defined as the number of events throughout the cell surface over the course of a time-lapse experiment, which was typically 3 minutes. Cell surface evaluation was carried out using ImageJ/Fiji segmentation tools [24]. Number of analyzed cells per labeled population is indicated.

Photo-bleaching correction

We implemented an optional custom-written correction based on a non-fitting, pixel-by-pixel weighted detrending method. Upon activation, the fluorescent time series is immediately processed so that users can review the intensity correction. In detail, for each pixel P_{xy}, we measured the fluorescence intensity difference between the first P_{xy0} and last P_{xyt} frame in the image series. These values were then normalized by the difference between the maximum μ_{max} and minimum μ_{min} intensity, also calculated throughout the image series to generate a weight map such as:

$$W_{xy} = \frac{(P_{xy0} - P_{xyt})}{(\mu_{max} - \mu_{min})}$$

Next, for each frame i we calculated the difference d_i between the mean intensity of the entire image series μ and the mean intensity of that frame μ_i. Finally, the fluorescence intensity of every pixel at each frame is compensated by $W_{xy}\, d_i$ to obtain the final detrended image series.

Statistical data analysis

We performed statistical analysis using Prism 9.0 (GraphPad). For multiple comparisons between populations of labeled vesicles, Kruskal-Wallis non-parametric ANOVA was used to determine significance, followed by Dunn's post hoc test. Statistical significance was considered for $\alpha = 0.05$ and only statistical differences are indicated. Data are reported as Box and whisker plots. Boxes show the median +/- interquartile range and the whiskers go down to the minimum and up to the maximum value in each dataset. Median value for each population is displayed in brackets below each corresponding box and whisker plot.

Results and Discussion

A user-configurable algorithm to automate the detection of fusion events

To assess the capacity of our algorithm at detecting fusion events, we focused on tagging the vesicle luminal cargos or vesicular membrane proteins with pHluorin [10]. The FP pHluorin is quenched in the acidic vesicular lumen, and brightens in the neutral extracellular environment upon vesicle fusion with the PM (Figure 2A). To image pHluorin-coupled reporters, TIRF microscopy has become the imaging modality of choice due to its inherent high signal-to-noise ratio with a reduced phototoxicity while increasing temporal resolution [8, 10, 44, 45]. The subsequent evanescent field of illumination enabled us to detect events close to the PM, minimizing the disturbance coming from fluorescently-labeled vesicles in the cytosplam. Using TIRF microscopy, the fusion event appears as an abrupt brightening followed by spreading of the fluorescence signal (Figure 2B). We focused on Hela cells expressing pHluorin-tagged CD9, CD63 and CD81 TSPANs commonly used as extracellular vesicle (EV) markers [34, 35, 46–48], and v-SNARE VAMP2 and VAMP7 proteins which are instrumental components in the fusion machineries in many cellular contexts [49–53] (Figure 2A-B). We noticed that cells expressing v-SNARE-pHluorin displayed a higher background intensity in the cytoplasm than those expressing TSPAN-pHluorin (Figure 2B). To account for the different image quality and/or fusion reporter signal intensity, we iteratively refined the detection parameters for fusion events reported with TSPAN and v-SNARE proteins (Supplementary Material 1) until we reached a plateau of detected fusion events. Specifically, we first optimized the detection threshold values $k\sigma_{wavelet}$ (Figure 1B) and dF/σ_{dF} (Figure 1D) to capture all candidate fusion events. We imposed a minimal signal duration of two frames to fulfil the Nyquist criteria. We completed the detection of candidate events with additional frames corresponding to 1 s (resp. 3-4 s) before (resp. after) the maximal peak fluorescence at t_0. The peak fluorescence profiles were fitted with a minimal number of five points and a minimal goodness-of-fit R^2 of 0.75 were set as the fitting threshold. No further adjustments were made before running the identification process. We reported a total number of 481 and 315 events for TSPAN and v-SNARE population respectively (Figure 2C). After reviewing the results, we eventually removed 10 TSPAN-pHluorin (2.1 % of total events) and 2 v-SNARE-pHluorin (0.6 % of total events) detection hits that did not correspond to fusion events but rather to filopodia tips coming in and out of focus, extracellular fluorescent objects and stationary vesicles. The identification error rate was

comparable or better than previously published algorithms [22, 23]. The capacity to modulate the identification algorithm ensured our tool to be adaptive in detecting fusion events.

Feature evaluation provides insights into distinct forms of vesicle-mediated exocytosis.

We next sought to investigate the exocytic dynamics of vesicle subpopulations. TSPAN CD9, CD63 and CD81 are known to form protein microdomains at the PM [54, 55] regulating various cellular function ranging from cell adhesion to proliferation [56] and signaling at the immune synapse [57]. Recently, these three TSPANs are found to be enriched to various degrees in the membrane of EV subpopulations such as ectosomes and exosomes. Exosomes are formed as intraluminal vesicles in late endosomes. Their secretion can be detected using pHluorin-tagged proteins upon fusion of acidic late endosomes with the PM [32, 34, 35, 41, 46, 48] (Figure 2A). Previous studies have, however, found CD9 mainly enriched in other subtypes of EVs directly budding from the plasma membrane and hence not monitored by our approach [35, 41, 48]. Using our algorithm, we examined post-fusion features of TSPAN subpopulations and compared them to transport vesicles reported with v-SNARE-pHluorin. In Hela cells, the detection algorithm recorded a statistically similar fusion activity between individual reporter populations varying between 3.0 and 5.5 (in $\mu m^{-2}.min^{-2}.10^{3}$; Figure 2C) with no correlation with the fusion apparent size and intensity (Figure 2D-E). The quantitative estimation of apparent size of events reported by TSPAN-pHluorin (CD9: 0.153 nm, CD63: 0.150, CD81: 0.147 nm; Figure 2D) were consistent with previous qualitative analysis at supra-optical electron microscopy (EM) resolution using a dynamic correlative light electron microscopy approach [41]. Interestingly, the apparent size did not differ significantly from v-SNARE-pHluorin-reported vesicles fusing with the PM (VAMP2: 0.145 nm, VAMP7: 0.149 nm; Figure 2D) which was at the lower end of the total spectrum previously reported by Altick and colleagues [58], but closely matching early quantitative EM studies in the central nervous system [59]. The advent of fast-imaging Structured Illumination Microscopy (SIM) may improve the recording of the structural dynamics of exocytosis with unprecedented resolution [60–63].

Focusing on the fusion duration, we first noted the short-lived fluorescence signal of VAMP2- and VAMP7-pHluorin, corresponding to a rapid either post-fusion lateral diffusion at the PM or endocytic process [10, 22, 41] (Figure 2F). In contrast, CD63 and CD81 subpopulations exhibited longer bursts of fluorescence signal which may correspond to the externalization of exosomes

(Figure 2F). We also showed that the subpopulations of tetraspanin displayed a significantly distinct fusion event duration (Figure 2F). The signal duration at the PM of CD81-pHluorin was almost two- and three-fold longer than CD63- and CD9-pHluorin respectively which could not previously be evaluated with this level of accuracy [41]. The divergence in fusion duration could not be explained by a noticeable difference in fusion event size, nor a significantly higher amount of TSPANs (Figure 2D-E). For CD63 and CD81, we hypothesized that this difference could reflect the heterogeneity in the composition, the biogenesis and/or the maturation of reported EV subpopulations. Indeed, TSPANs are known to organize in distinct TSPAN-enriched microdomains that consist primarily of less than 120 nm homotypic TSPAN-TSPAN interactions and specific partner proteins [64–66] and mark distinct populations of exosomes [67]. Furthermore, the signal duration of CD9-pHluorin was similar to v-SNARE-labeled population of vesicles, as previously observed [41]. This suggested that CD9-pHluorin bursts of fluorescence may reflect post-fusion lateral diffusion of CD9-pHluorin over the PM similarly to v-SNARE-pHluorin rather than exosome secretion in the majority of events.

Altogether, our computer vision-assisted tool enabled us to identify exocytosis events for different types of cargo, different types of vesicles, but also to record features, providing insights into post-fusion dynamics.

Conclusion

We have developed a user-friendly and efficient ImageJ2/Fiji plugin to supervise the automated detection of fusion events on a single-cell basis. A major strength of our approach is that the identification algorithm can be adjusted to account for differences in image quality and/or dynamics of exocytosis fluorescent reporters. We illustrated the capacity of our tool by visualizing and quantifying fusion events reported with either TSPAN or v-SNARE reporters both coupled to pHluorin. Our tool was capable to discriminate various vesicular population depending on the fusion intensity or/and duration. In addition, the computer-vision assisted plugin includes tools to investigate features of single exocytic event including the apparent size, duration, intensity and localisation. We reason that the ExoJ plugin would be a useful tool for providing direct insight into exocytosis dynamics.

Availability and requirements

Project name: ExoJ, a tool for quantitative imaging of exocytosis

Project home page: https://www.project-exoj.com/

Operating system(s): ImageJ2/Fiji

Programming language: Java

Other requirements: Java 8.0

License: GPLv3 license

Any restrictions to use by non-academics: none

Availability of data and Material

The datasets used and/or analysed during the current study are available from the corresponding authors on reasonable request. Time series are available for testing on the Zenodo repository: https://zenodo.org/record/6610894

The plugin ExoJ as well as documentation can be found on the following website https://www.project-exoj.com/

Acknowledgements and Funding

We acknowledge the NeurImag imaging facility of the Institute of Psychiatry and Neurosciences of Paris (Inserm U1266) where the imaging experiments were carried out. We are grateful to Sésame Région Ile-de-France for the funding of the Zeiss Confocal LSM 880 equipped with a TIRF module. We would like to thank Julie N'guyen for maintaining and providing HeLa cells, and Sebastien Nola for his insightful comments on the manuscript. This work was funded by Agence Nationale de la Recherche (ANR-19-HBPR-0003) and FLAG-ERA (Sensei grant 19-CE16-0012-01) to L.D, by a European Molecular Biology Organization grant (EMBO ALTF 1383-2014), a Fondation ARC pour la Recherche sur le Cancer fellowship (PJA 20161204808) to F.J.V., a

Fondation pour la Recherche Médicale grant (AJE20160635884) to G.V.N and an Institut National Du Cancer grant (INCA N°2019-125 PLBIO19-059) to F.J.V. and G.V.N.

Author contributions

JL: Conceptualization, Software, Data curation, Resources, Visualization, Writing- Original draft, Writing- Review and Editing. **FJV**: Resources, Investigation, Validation, Writing-Review and Editing. **GVN**: Supervision, Funding acquisition, Writing-Review and Editing. **LD**: Conceptualization, Supervision, Funding acquisition, Resources, Investigation, Writing-Review and Editing. **PB**: Conceptualization, Software, Data curation, Investigation, Formal analysis, Visualization, Writing-Original draft, Writing-Review and Editing.

Abbreviations

PM: Plasma membrane

TIRF: Total Internal Reflection Fluorescence

FP: Fluorescent protein

MAD: Median absolute deviation

RGB: Red green blue

VAMP2: Vesicle-associated membrane protein 2

VAMP7/TI-VAMP: Vesicle-associated membrane protein 7 / Tetanus neurotoxin-Insensitive vesicle-associated membrane protein

EV: Extracellular vesicle

EM: Electron microscopy

SIM: Structured illumination microscopy

Figure legends

Figure 1. **User-configurable parameters for the identification of fusion events**.

(A) The framework of the algorithm comprises three main steps. A typical fusion event labeled by CD9-pHluorin in Hela cell is shown as a time-lapse montage. Before fusion (gray), the fluorescence is quenched in acidic environment. Upon fusion, the pHluorin is exposed to neutral pH. A bright diffraction-limited spot appears and diffuses over time (blue), reported by the mean lifetime τ. **(B)** Vesicles (seen as spots) are detected using either a local maxima or *à trous wavelet transform* algorithm (default option). The detection threshold value is manually set by users to permit the algorithm to detect spots on single images (here in red). The threshold value is a multiple of the Mediane Absolute Deviation (MAD) of $C_{wavelet}$. **(C)** Previously detected spots are connected to reconstruct time-lapse trajectories. Parameters considered for reconstruction are illustrated. Tracking results including intensity profile and fluorescent montage for single candidate events can be reviewed upon selection of Show Event List button. **(D)** For each candidate fusion event, a series of measurements are made: the local background F_0 (1); the fluorescence peak profile was fitted with a negative exponential function to derive the mean lifetime τ (2-5); σ_{dF}, the MAD of the 1st order differential fluorescence intensity profile (6); the fluorescence intensities at the different time points were fitted with a two-dimensional Gaussian fit to estimate the apparent radius of the fusion event (7, 9) and the XY position (8).

Figure 2. Feature measurements of single vesicle population evidenced distinct form of vesicle-mediated exocytosis

(A) Schematic model illustrating the markers used in this study to monitor vesicle fusion to the PM. **(B)** Time-lapse montages of fusion events reported by TSPAN and v-SNARE proteins (fire LUT). **(C-F)** Combined Scatter dot (black) and Box and Whisker (red) plots are shown for individual population of labeled vesicles. The median values of fusion **(C)** activity, **(D)** normalized peak intensity ($\Delta F/F_0$), **(E)** apparent size and **(F)** event duration are displayed in brackets. **(C)** Number of analyzed cells (N) as well as the total number of fusion events (n) for the two families of proteins are indicated (in details: CD9, n = 129; CD63, n = 200; CD81, n =

152; Vamp2, n = 232; Vamp7, n = 83). **(D)** Comparison between TSPAN- and v-SNARE-labeled vesicular population was performed using a Kruskal-wallis's test ($P < 0.0001$) followed with a post hoc Dunn's multiple comparison test (****, $P < 0.0001$; ***, $P < 0.0002$). **(E)** Kruskal-wallis's test was performed ($P < 0.005$) followed with a post hoc Dunn's multiple comparison test (*, $P < 0.04$). **(F)** Kruskal-wallis's test was performed ($P < 0.0001$) followed with a post hoc Dunn's multiple comparison test (****, $P < 0.0001$; ***, $P < 0.0002$; *, $P < 0.03$).

Figure S1. Reporting analysis of fusion events.

(A) Series of measurements on single fusion events are summarized in a result table, including the XY location, the onset time (peak frame), the maximal displacement during the fusion event, the detection threshold value (dF/σ_{dF}), the local background (F_0) and peak fluorescence intensity (ΔF), the estimated apparent size (est. radius) and mean lifetime decay (τ). Corresponding graphs are displayed for each fusion event. **(B)** Histograms of distribution of fusion event duration (Mean lifetime decay τ), apparent size (Estimated radius) and temporal occurrence (Event counts) at the single cell level can be generated upon selection. A spatial occurrence map (Distribution map) is also available for export.

Table legends

Table 1. General command

Available tools along the identification and analysis process

Table 2. Spot detection

Parameters and options for vesicle (seen as spot) detection

Table 3. Spot tracking

Parameters and options for vesicle (seen as spot) tracking

Table 4. Event identification

Parameters and options for the identification of vesicle fusion events

Supplementary Materials

File 1. Configuration file for the identification of TSPAN-labeled fusion events.

File 2. Configuration file for the identification of v-SNARE-labeled fusion events.

References

1. Verhage M, Sørensen JB. Vesicle Docking in Regulated Exocytosis. Traffic. 2008;9:1414–24.

2. Guček A, Gandasi NR, Omar-Hmeadi M, Bakke M, Døskeland SO, Tengholm A, et al. Fusion pore regulation by cAMP/Epac2 controls cargo release during insulin exocytosis. Elife. 2019;8.

3. Gundelfinger ED, Kessels MM, Qualmann B. Temporal and spatial coordination of exocytosis and endocytosis. Nat Rev Mol Cell Biol. 2003;4:127–39.

4. Chen YA, Scheller RH. SNARE-mediated membrane fusion. Nat Rev Mol Cell Biol. 2001;2:98–106.

5. Bebelman MP, Smit MJ, Pegtel DM, Baglio SR. Biogenesis and function of extracellular vesicles in cancer. Pharmacol Ther. 2018;188:1–11.

6. Lamichhane TN, Sokic S, Schardt JS, Raiker RS, Lin JW, Jay SM. Emerging Roles for Extracellular Vesicles in Tissue Engineering and Regenerative Medicine. Tissue Eng Part B Rev. 2015;21:45–54.

7. Meldolesi J. Exosomes and Ectosomes in Intercellular Communication. Current Biology. 2018;28:R435–44.

8. van Niel G, D'Angelo G, Raposo G. Shedding light on the cell biology of extracellular vesicles. Nat Rev Mol Cell Biol. 2018;19:213–28.

9. Ge S, Koseoglu S, Haynes CL. Bioanalytical tools for single-cell study of exocytosis. Anal Bioanal Chem. 2010;397:3281–304.

10. Miesenböck G, de Angelis DA, Rothman JE. Visualizing secretion and synaptic transmission with pH-sensitive green fluorescent proteins. Nature. 1998;394:192–5.

11. Sankaranarayanan S, de Angelis D, Rothman JE, Ryan TA. The Use of pHluorins for Optical Measurements of Presynaptic Activity. Biophys J. 2000;79:2199–208.

12. Burchfield JG, Lopez JA, Mele K, Vallotton P, Hughes WE. Exocytotic Vesicle Behaviour Assessed by Total Internal Reflection Fluorescence Microscopy. Traffic. 2010;11:429–39.

13. Bebelman MP, Bun P, Huveneers S, van Niel G, Pegtel DM, Verweij FJ. Real-time imaging of multivesicular body–plasma membrane fusion to quantify exosome release from single cells. Nat Protoc. 2020;15:102–21.

14. Schmoranzer J, Goulian M, Axelrod D, Simon SM. Imaging Constitutive Exocytosis with Total Internal Reflection Fluorescence Microscopy. Journal of Cell Biology. 2000;149:23–32.

15. Liu A, Huang X, He W, Xue F, Yang Y, Liu J, et al. pHmScarlet is a pH-sensitive red fluorescent protein to monitor exocytosis docking and fusion steps. Nat Commun. 2021;12:1413.

16. Shen Y, Rosendale M, Campbell RE, Perrais D. pHuji, a pH-sensitive red fluorescent protein for imaging of exo- and endocytosis. Journal of Cell Biology. 2014;207:419–32.

17. Martineau M, Somasundaram A, Grimm JB, Gruber TD, Choquet D, Taraska JW, et al. Semisynthetic fluorescent pH sensors for imaging exocytosis and endocytosis. Nat Commun. 2017;8:1412.

18. Sankaranarayanan S, de Angelis D, Rothman JE, Ryan TA. The Use of pHluorins for Optical Measurements of Presynaptic Activity. Biophys J. 2000;79:2199–208.

19. Persoon CM, Hoogstraaten RI, Nassal JP, van Weering JRT, Kaeser PS, Toonen RF, et al. The RAB3-RIM Pathway Is Essential for the Release of Neuromodulators. Neuron. 2019;104:1065-1080.e12.

20. Diaz E, Ayala G, Diaz ME, Liang-Wei Gong, Toomre D. Automatic Detection of Large Dense-Core Vesicles in Secretory Cells and Statistical Analysis of Their Intracellular Distribution. IEEE/ACM Trans Comput Biol Bioinform. 2010;7:2–11.

21. Sebastian R, Diaz M-E, Ayala G, Letinic K, Moncho-Bogani J, Toomre D. Spatio-Temporal Analysis of Constitutive Exocytosis in Epithelial Cells. IEEE/ACM Trans Comput Biol Bioinform. 2006;3:17–32.

22. Urbina FL, Gomez SM, Gupton SL. Spatiotemporal organization of exocytosis emerges during neuronal shape change. Journal of Cell Biology. 2018;217:1113–28.

23. Yuan T, Lu J, Zhang J, Zhang Y, Chen L. Spatiotemporal Detection and Analysis of Exocytosis Reveal Fusion “Hotspots” Organized by the Cytoskeleton in Endocrine Cells. Biophys J. 2015;108:251–60.

24. Schindelin J, Arganda-Carreras I, Frise E, Kaynig V, Longair M, Pietzsch T, et al. Fiji: an open-source platform for biological-image analysis. Nat Methods. 2012;9:676–82.

25. Linkert M, Rueden CT, Allan C, Burel J-M, Moore W, Patterson A, et al. Metadata matters: access to image data in the real world. Journal of Cell Biology. 2010;189:777–82.

26. Wu L-G, Hamid E, Shin W, Chiang H-C. Exocytosis and Endocytosis: Modes, Functions, and Coupling Mechanisms. Annu Rev Physiol. 2014;76:301–31.

27. Miura K. Bleach correction ImageJ plugin for compensating the photobleaching of time-lapse sequences. F1000Res. 2020;9:1494.

28. Olivo-Marin J-C. Extraction of spots in biological images using multiscale products. Pattern Recognit. 2002;35:1989–96.

29. Crocker JC, Grier DG. Methods of Digital Video Microscopy for Colloidal Studies. J Colloid Interface Sci. 1996;179:298–310.

30. Chenouard N, Smal I, de Chaumont F, Maška M, Sbalzarini IF, Gong Y, et al. Objective comparison of particle tracking methods. Nat Methods. 2014;11:281–9.

31. Bowser DN, Khakh BS. Two forms of single-vesicle astrocyte exocytosis imaged with total internal reflection fluorescence microscopy. Proceedings of the National Academy of Sciences. 2007;104:4212–7.

32. Escola J-M, Kleijmeer MJ, Stoorvogel W, Griffith JM, Yoshie O, Geuze HJ. Selective Enrichment of Tetraspan Proteins on the Internal Vesicles of Multivesicular Endosomes and on Exosomes Secreted by Human B-lymphocytes. Journal of Biological Chemistry. 1998;273:20121–7.

33. Yáñez-Mó M, Siljander PR-M, Andreu Z, Bedina Zavec A, Borràs FE, Buzas EI, et al. Biological properties of extracellular vesicles and their physiological functions. J Extracell Vesicles. 2015;4:27066.

34. Théry C, Witwer KW, Aikawa E, Alcaraz MJ, Anderson JD, Andriantsitohaina R, et al. Minimal information for studies of extracellular vesicles 2018 (MISEV2018): a position statement of the International Society for Extracellular Vesicles and update of the MISEV2014 guidelines. J Extracell Vesicles. 2018;7:1535750.

35. Kowal J, Arras G, Colombo M, Jouve M, Morath JP, Primdal-Bengtson B, et al. Proteomic comparison defines novel markers to characterize heterogeneous populations of extracellular vesicle subtypes. Proceedings of the National Academy of Sciences. 2016;113.

36. Söllner T, Whiteheart SW, Brunner M, Erdjument-Bromage H, Geromanos S, Tempst P, et al. SNAP receptors implicated in vesicle targeting and fusion. Nature. 1993;362:318–24.

37. Galli T, Zahraoui A, Vaidyanathan V v., Raposo G, Tian JM, Karin M, et al. A Novel Tetanus Neurotoxin-insensitive Vesicle-associated Membrane Protein in SNARE Complexes of the Apical Plasma Membrane of Epithelial Cells. Mol Biol Cell. 1998;9:1437–48.

38. Südhof TC, Rothman JE. Membrane Fusion: Grappling with SNARE and SM Proteins. Science (1979). 2009;323:474–7.

39. Chaineau M, Danglot L, Galli T. Multiple roles of the vesicular-SNARE TI-VAMP in post-Golgi and endosomal trafficking. FEBS Lett. 2009;583:3817–26.

40. Galli T, Tareste D. SNAREs: Membrane Fusion and Beyond. In: Reference Module in Life Sciences. Elsevier; 2022.

41. Verweij FJ, Bebelman MP, Jimenez CR, Garcia-Vallejo JJ, Janssen H, Neefjes J, et al. Quantifying exosome secretion from single cells reveals a modulatory role for GPCR signaling. Journal of Cell Biology. 2018;217:1129–42.

42. Chaineau M, Danglot L, Proux-Gillardeaux V, Galli T. Role of HRB in Clathrin-dependent Endocytosis. Journal of Biological Chemistry. 2008;283:34365–73.

43. Danglot L, Zylbersztejn K, Petkovic M, Gauberti M, Meziane H, Combe R, et al. Absence of TI-VAMP/Vamp7 Leads to Increased Anxiety in Mice. Journal of Neuroscience. 2012;32:1962–8.

44. Axelrod D, Omann GM. Combinatorial microscopy. Nat Rev Mol Cell Biol. 2006;7:944–52.

45. Mattheyses AL, Simon SM, Rappoport JZ. Imaging with total internal reflection fluorescence microscopy for the cell biologist. J Cell Sci. 2010;123:3621–8.

46. Crescitelli R, Lässer C, Szabó TG, Kittel A, Eldh M, Dianzani I, et al. Distinct RNA profiles in subpopulations of extracellular vesicles: apoptotic bodies, microvesicles and exosomes. J Extracell Vesicles. 2013;2:20677.

47. Witwer KW, Théry C. Extracellular vesicles or exosomes? On primacy, precision, and popularity influencing a choice of nomenclature. J Extracell Vesicles. 2019;8:1648167.

48. Mathieu M, Névo N, Jouve M, Valenzuela JI, Maurin M, Verweij FJ, et al. Specificities of exosome versus small ectosome secretion revealed by live intracellular tracking of CD63 and CD9. Nat Commun. 2021;12:4389.

49. Jahn R, Scheller RH. SNAREs — engines for membrane fusion. Nat Rev Mol Cell Biol. 2006;7:631–43.

50. Kesavan J, Borisovska M, Bruns D. v-SNARE Actions during Ca2+-Triggered Exocytosis. Cell. 2007;131:351–63.

51. Verderio C, Cagnoli C, Bergami M, Francolini M, Schenk U, Colombo A, et al. TI-VAMP/VAMP7 is the SNARE of secretory lysosomes contributing to ATP secretion from astrocytes. Biol Cell. 2012;104:213–28.

52. Ligeon L-A, Moreau K, Barois N, Bongiovanni A, Lacorre D-A, Werkmeister E, et al. Role of VAMP3 and VAMP7 in the commitment of *Yersinia pseudotuberculosis* to LC3-associated pathways involving single- or double-membrane vacuoles. Autophagy. 2014;10:1588–602.

53. Han J, Pluhackova K, Böckmann RA. The Multifaceted Role of SNARE Proteins in Membrane Fusion. Front Physiol. 2017;8.

54. Hemler ME. Tetraspanin functions and associated microdomains. Nat Rev Mol Cell Biol. 2005;6:801–11.

55. le Naour F, André M, Boucheix C, Rubinstein E. Membrane microdomains and proteomics: Lessons from tetraspanin microdomains and comparison with lipid rafts. Proteomics. 2006;6:6447–54.

56. Becic A, Leifeld J, Shaukat J, Hollmann M. Tetraspanins as Potential Modulators of Glutamatergic Synaptic Function. Front Mol Neurosci. 2022;14.

57. Levy S, Shoham T. The tetraspanin web modulates immune-signalling complexes. Nat Rev Immunol. 2005;5:136–48.

58. Altick AL, Baryshnikova LM, Vu TQ, von Bartheld CS. Quantitative analysis of multivesicular bodies (MVBs) in the hypoglossal nerve: Evidence that neurotrophic factors do not use MVBs for retrograde axonal transport. J Comp Neurol. 2009;514:641–57.

59. Roizin L, Nishikawa K, Koizumi J, Keoseian S. The Fine Structure of the Multivesicular Body and Their Relationship to the Ultracellular Constituents of the Central Nervous System [*] [†]. J Neuropathol Exp Neurol. 1967;26:223–49.

60. Li D, Shao L, Chen B-C, Zhang X, Zhang M, Moses B, et al. Extended-resolution structured illumination imaging of endocytic and cytoskeletal dynamics. Science (1979). 2015;349.

61. Huang X, Fan J, Li L, Liu H, Wu R, Wu Y, et al. Fast, long-term, super-resolution imaging with Hessian structured illumination microscopy. Nat Biotechnol. 2018;36:451–9.

62. Roth J, Mehl J, Rohrbach A. Fast TIRF-SIM imaging of dynamic, low-fluorescent biological samples. Biomed Opt Express. 2020;11:4008.

63. Liu A, Huang X, He W, Xue F, Yang Y, Liu J, et al. pHmScarlet is a pH-sensitive red fluorescent protein to monitor exocytosis docking and fusion steps. Nat Commun. 2021;12:1413.

64. Charrin S, le Naour F, Silvie O, Milhiet P-E, Boucheix C, Rubinstein E. Lateral organization of membrane proteins: tetraspanins spin their web. Biochemical Journal. 2009;420:133–54.

65. Rubinstein E, le Naour F, Lagaudrière-Gesbert C, Billard M, Conjeaud H, Boucheix C. CD9, CD63, CD81, and CD82 are components of a surface tetraspan network connected to HLA-DR and VLA integrins. Eur J Immunol. 1996;26:2657–65.

66. van Deventer S, Arp AB, van Spriel AB. Dynamic Plasma Membrane Organization: A Complex Symphony. Trends Cell Biol. 2021;31:119–29.

67. Matsui T, Osaki F, Hiragi S, Sakamaki Y, Fukuda M. ALIX and ceramide differentially control polarized small extracellular vesicle release from epithelial cells. EMBO Rep. 2021;22.

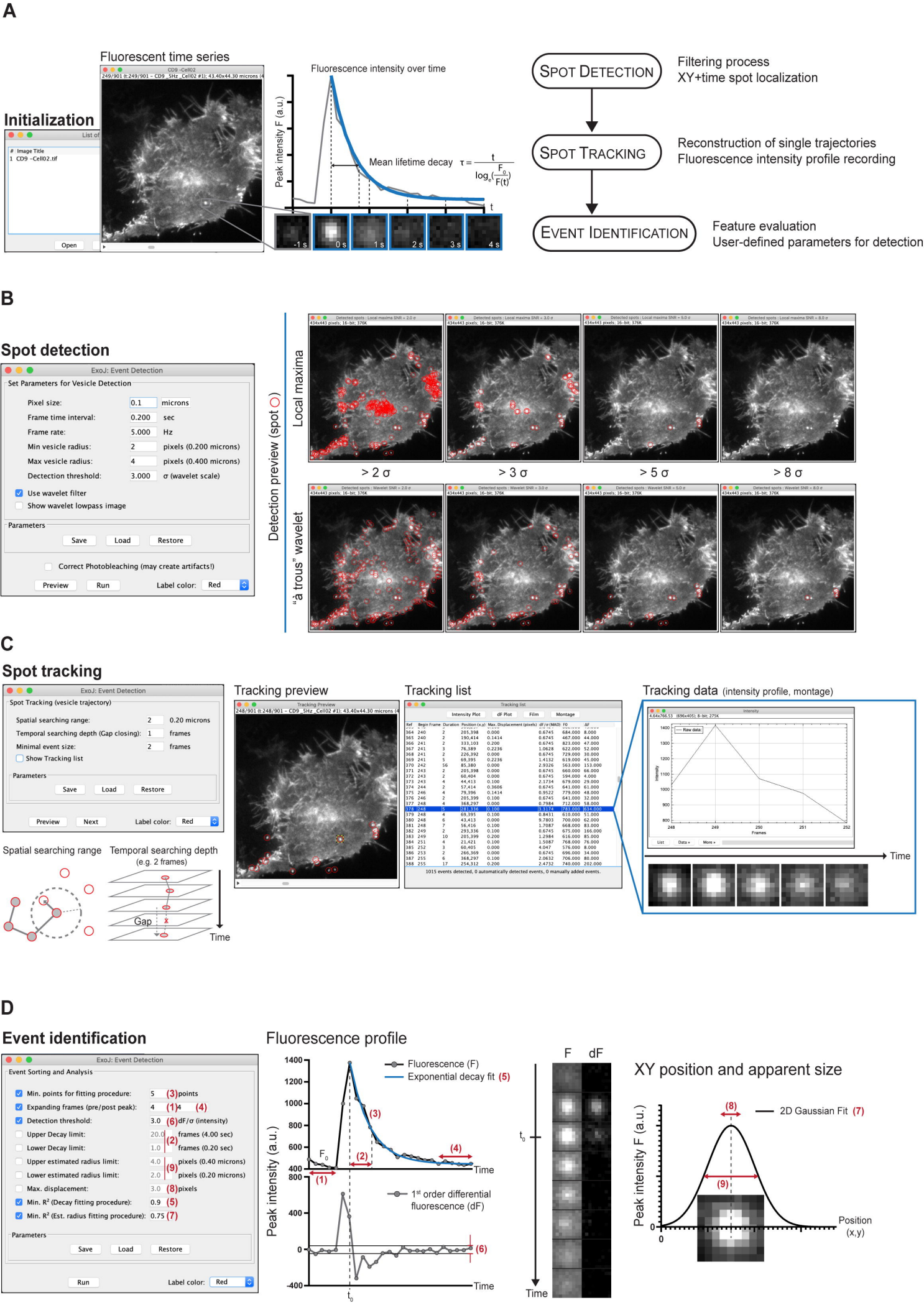
A
Fluorescent time series
Initialization
Fluorescence intensity over time
Peak intensity F (a.u.)
Mean lifetime decay
-1 s
0 s
1 s
2 s
3 s
4 s
SPOT DETECTION
Filtering process
XY+time spot localization
SPOT TRACKING
Reconstruction of single trajectories
Fluorescence intensity profile recording
EVENT IDENTIFICATION
Feature evaluation
User-defined parameters for detection
B
Spot detection
ExoJ: Event Detection
Set Parameters for Vesicle Detection
Pixel size: 0.1 microns
Frame time interval: 0.200 sec
Frame rate: 5.000 Hz
Min vesicle radius: 2 pixels (0.200 microns)
Max vesicle radius: 4 pixels (0.400 microns)
Dectection threshold: 3.000 σ (wavelet scale)
Use wavelet filter
Show wavelet lowpass image
Parameters
Save
Load
Restore
Correct Photobleaching (may create artifacts!)
Preview
Run
Label color: Red
Detection preview (spot)
Local maxima
"à trous" wavelet
> 2 σ
> 3 σ
> 5 σ
> 8 σ
C
Spot tracking
ExoJ: Event Detection
Spot Tracking (vesicle trajectory)
Spatial searching range: 2 0.20 microns
Temporal searching depth (Gap closing): 1 frames
Minimal event size: 2 frames
Show Tracking list
Parameters
Save
Load
Restore
Preview
Next
Label color: Red
Spatial searching range
Temporal searching depth
(e.g. 2 frames)
Gap
Time
Tracking preview
Tracking list
Tracking data (intensity profile, montage)
Time
D
Event identification
ExoJ: Event Detection
Event Sorting and Analysis
Min. points for fitting procedure: 5 (3) points
Expanding frames (pre/post peak): 4 (1) 4 (4)
Detection threshold: 3.0 (6) dF/σ (intensity)
Upper Decay limit: 20.0 (2) frames (4.00 sec)
Lower Decay limit: 1.0 frames (0.20 sec)
Upper estimated radius limit: 4.0 (9) pixels (0.40 microns)
Lower estimated radius limit: 2.0 pixels (0.20 microns)
Max. displacement: 3.0 (8) pixels
Min. R² (Decay fitting procedure): 0.9 (5)
Min. R² (Est. radius fitting procedure): 0.75 (7)
Parameters
Save
Load
Restore
Run
Label color: Red
Fluorescence profile
Fluorescence (F)
Exponential decay fit (5)
Peak intensity (a.u.)
Time
1st order differential fluorescence (dF)
F
dF
XY position and apparent size
2D Gaussian Fit (7)
Peak intensity F (a.u.)
Position (x,y)

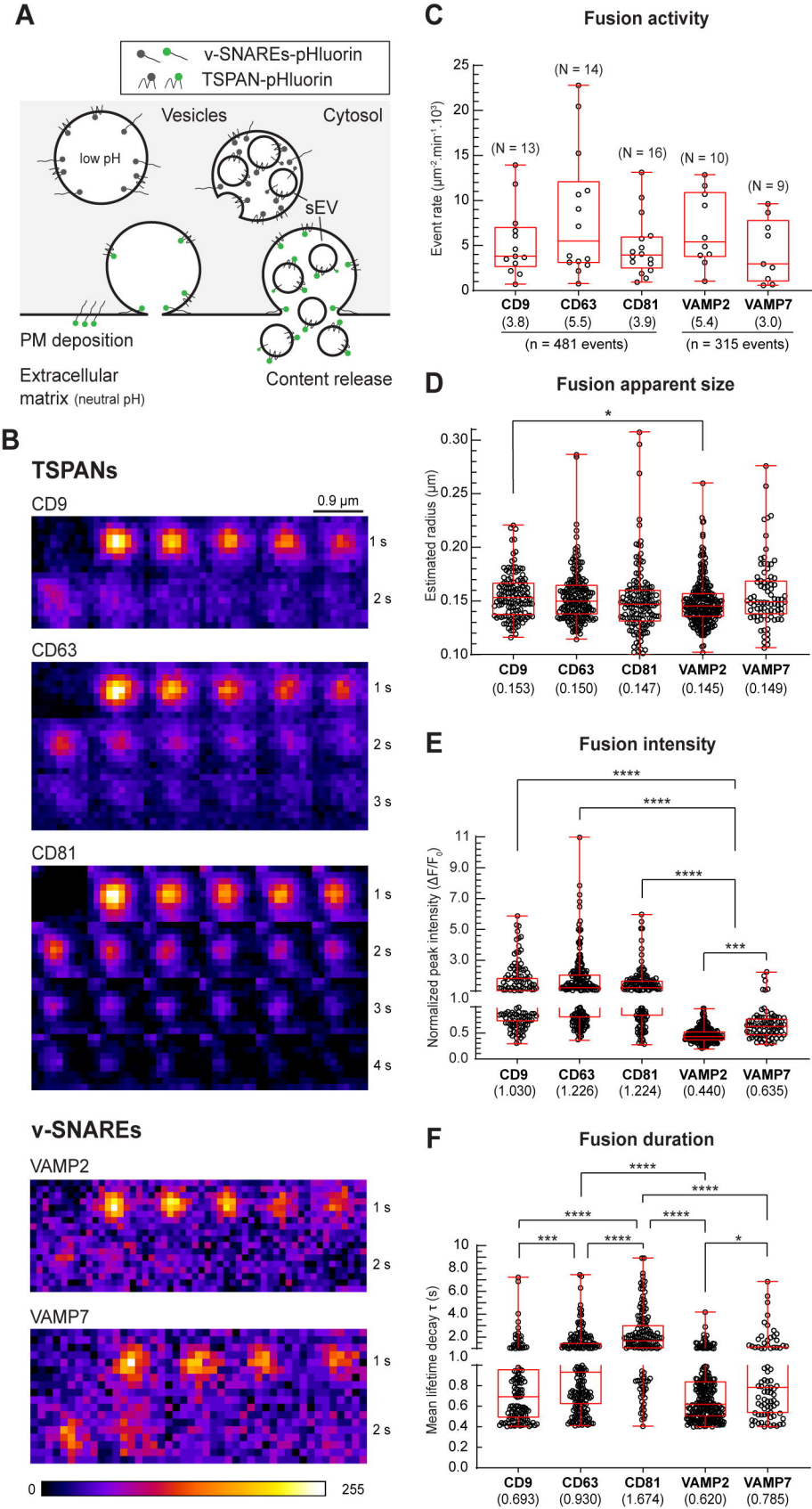
A
v-SNAREs-pHluorin
TSPAN-pHluorin
Vesicles
Cytosol
low pH
sEV
PM deposition
Extracellular matrix (neutral pH)
Content release
B
TSPANs
CD9
0.9 µm
1 s
2 s
CD63
1 s
2 s
3 s
CD81
1 s
2 s
3 s
4 s
v-SNAREs
VAMP2
1 s
2 s
VAMP7
1 s
2 s
0
255
C
Fusion activity
Event rate (µm⁻².min⁻¹.10³)
(N = 13)
(N = 14)
(N = 16)
(N = 10)
(N = 9)
CD9 (3.8)
CD63 (5.5)
CD81 (3.9)
VAMP2 (5.4)
VAMP7 (3.0)
(n = 481 events)
(n = 315 events)
D
Fusion apparent size
Estimated radius (µm)
CD9 (0.153)
CD63 (0.150)
CD81 (0.147)
VAMP2 (0.145)
VAMP7 (0.149)
E
Fusion intensity
Normalized peak intensity (ΔF/F0)
CD9 (1.030)
CD63 (1.226)
CD81 (1.224)
VAMP2 (0.440)
VAMP7 (0.635)
F
Fusion duration
Mean lifetime decay τ (s)
CD9 (0.693)
CD63 (0.930)
CD81 (1.674)
VAMP2 (0.620)
VAMP7 (0.785)

A

List of detected fusion events

Intracellular XY location

XY tracking over time

Radius profiles

Sequence

Fluorescence peak intensity (F)

1st-order differential peak intensity (dF)

Mean radial intensity (Spatial dynamics)

Center (1 pixel)
1st ring
2nd ring
3rd ring
4th ring
5th ring
6th ring

Fusion

Mask

B

Distribution map

Mean lifetime distribution

Apparent size distribution

Temporal occurence

(Pop-up window) **List of available files**	Upon starting the plugin, a pop-up window lists opened image-type files. To start (resp. stop) the analysis, press **Open** (resp. **Close**). If an image series does not appear, **Refresh** the pop-up window. After pressing **Open**, the selected image series will be duplicated for further processing and analysis. Note that the plugin can run in parallel multiple instances.
Save, **Load**, **Restore**	Parameters are saved (in .dat format), loaded (.dat file) or restored to the metadata of the image series.
Label color	Detected vesicles (seen as spots) are marked by colored-circles (drop-down menu). Color can be chosen here.
Preview, **Run**	At each step, processing results can be reviewed for different set of parameters (**Preview**). During the spot detection step, single fluorescent images are displayed. During the spot tracking step, the whole sequence is shown. During the event identification step, the whole sequence and the table result are displayed. To proceed to the next step, press **Run**.

Pixel size, **Frame rate**, **Frame time interval**	Read the metadata of the image series regarding the spatial and temporal information.	
Min., Max. vesicle radius	Initial entries for the estimated radius (in pixel) of the vesicular population of interest. A minimal value of 2 pixels is recommended.	
(Checked) **Use wavelet filter**	Prior to the spot detection, the background of the image series was subtracted using the *à trous wavelet transform* algorithm. The wavelet coefficient ($C_{wavelet}$) is evaluated according to the initial user-entry for vesicle radius range.	
	Detection threshold	Critical integer value that corresponds to a multiple of $\sigma_{wavelet}$, calculated as the MAD of $C_{wavelet}$. For a high (resp. low) value, number of detected spots is decreasing (resp. increasing) along with the calculation time.
	Show lowpass image	When activated, this option displays single fluorescent images of spots with $C_{wavelet}$ above the **detection threshold**.
(Unchecked) **Use wavelet filter**	The spot detection relies on the local maxima algorithm with the **Min.** and **Max. vesicle radius** as initial entries.	
	Detection threshold	Critical integer value that corresponds to a multiple of $\sigma_{f\ (intensity)}$, calculated as the MAD of all pixel intensity at each image.
Correct Photobleaching	A pixel-by-pixel detrending method is immediately applied to the image series. Note that the correction can introduce bright/saturated pixels. The process can be reversed by deactivating the option.	

Spatial searching radius (in pixel)	This integer value corresponds to the maximal acceptable displacement of the spot (flagged by its fluorescence peak) between two consecutive frames. We recommend setting the value similar to the **Min. vesicle radius** (from Step 1) to account for possible movements during image acquisition (cell, imaging setup, …).
Temporal searching depth (in frame number)	This integer value corresponds to the maximal acceptable frame gap if the tracked spot disappears from one frame to the next. In this case, the algorithm will suppose that the given spot remains at the same position until it reappears in the following frames. The algorithm will hence generate virtual spots to fill the gap and assemble tracks. By default, the value 1 corresponds to a no gap situation.
Minimal event size (in frame number)	This threshold value corresponds to the minimal duration of each individual track that will be processed and analyzed (Event Detection and Analysis step). Note that gaps are not counted in the track size.
Show event list	When activated, the list of all vesicle trajectories is displayed in a pop-up window list where montages of still images, traces of F and dF can be generated and further saved.

Min. points for fitting procedure	Integer value that corresponds to the minimal number of points needed to fit the fluorescence decay intensity over time to derive the mean lifetime. The value should not be higher than the number of **Expanding frames (post peak)**.
Expanding frames (pre/post peak)	Addition of frames before and after peak detection. The two integer values influence the evaluation of $\sigma_{dF_intensity}$ (MAD of dF). We recommend considering a window of 1 second before peak detection (pre). Note that a large window after peak detection (post) improves the evaluation of mean lifetime decay but might hinder the detection of consecutive fusion events at the same location.
Detection threshold ($dF/\sigma_{dF_intensity}$)	Integer value above which the 1st order differential intensity peak (dF) is seen as a fusion event.
Upper/Lower decay limit	Integer range for the mean lifetime decay of candidate fusion events. A minimal value of 2 timepoints is recommended to fulfill Nyquist criteria.
Upper/Lower estimated radius limit	Integer range for the estimated radius of candidate fusion events.
Max. displacement	Maximal lateral shift of the peak intensity (F) measured throughout the fusion event process.
Min. R^2	Fitted curves for deriving the mean lifetime and the estimated radius of the fusion event with a minimal goodness-of-fit R^2